

# Nonlinear ultrasound simulation in an axisymmetric coordinate system using a $k$ -space pseudospectral method

Bradley E. Treeby, Elliott S. Wise, Filip Kuklis, Jiri Jaros, and B. T. Cox

Citation: *The Journal of the Acoustical Society of America* **148**, 2288 (2020); doi: 10.1121/10.0002177

View online: <https://doi.org/10.1121/10.0002177>

View Table of Contents: <https://asa.scitation.org/toc/jas/148/4>

Published by the [Acoustical Society of America](#)

---

## ARTICLES YOU MAY BE INTERESTED IN

[A computational method whose time had come](#)

*The Journal of the Acoustical Society of America* **148**, R7 (2020); <https://doi.org/10.1121/10.0002055>

[Nonlinear wave propagation through multiple scattering media and virtual time reversal focusing](#)

*The Journal of the Acoustical Society of America* **148**, 1315 (2020); <https://doi.org/10.1121/10.0001887>

[Phase speed in water-saturated sand and glass beads at MHz frequencies](#)

*The Journal of the Acoustical Society of America* **148**, 2301 (2020); <https://doi.org/10.1121/10.0002250>

[A Fourier transform formulation for radiation from an un baffled cylinder](#)

*The Journal of the Acoustical Society of America* **148**, 2311 (2020); <https://doi.org/10.1121/10.0002258>

[Generalization of Sabine's reverberation theory](#)

*The Journal of the Acoustical Society of America* **148**, R5 (2020); <https://doi.org/10.1121/10.0001806>

[Acoustic source localization with the angular spectrum approach in continuously stratified media](#)

*The Journal of the Acoustical Society of America* **148**, EL333 (2020); <https://doi.org/10.1121/10.0002095>

---



CALL FOR PAPERS

**JASA**  
THE JOURNAL OF THE  
ACOUSTICAL SOCIETY OF AMERICA

**Special Issue:**  
**Lung Ultrasound**

The banner features a blue background with a grid pattern and a blurred image of a person's head and neck, likely representing lung ultrasound. The text is in white and yellow.

## Nonlinear ultrasound simulation in an axisymmetric coordinate system using a $k$ -space pseudospectral method<sup>a)</sup>

Bradley E. Treeby,<sup>1,b)</sup> Elliott S. Wise,<sup>1,c)</sup> Filip Kuklis,<sup>2</sup> Jiri Jaros,<sup>2,d)</sup> and B. T. Cox<sup>1,e)</sup>

<sup>1</sup>Department of Medical Physics and Biomedical Engineering, University College London, Gower Street, London WC1E 6BT, United Kingdom

<sup>2</sup>Centre of Excellence IT4Innovations, Faculty of Information Technology, Brno University of Technology, Božetěchova 2, Brno, 612 00, Czech Republic

### ABSTRACT:

A full-wave model for nonlinear ultrasound propagation through a heterogeneous and absorbing medium in an axisymmetric coordinate system is developed. The model equations are solved using a nonstandard or  $k$ -space pseudospectral time domain method. Spatial gradients in the axial direction are calculated using the Fourier collocation spectral method, and spatial gradients in the radial direction are calculated using discrete trigonometric transforms. Time integration is performed using a  $k$ -space corrected finite difference scheme. This scheme is exact for plane waves propagating linearly in the axial direction in a homogeneous and lossless medium and significantly reduces numerical dispersion in the more general case. The implementation of the model is described, and performance benchmarks are given for a range of grid sizes. The model is validated by comparison with several analytical solutions. This includes one-dimensional absorption and nonlinearity, the pressure field generated by plane-piston and bowl transducers, and the scattering of a plane wave by a sphere. The general utility of the model is then demonstrated by simulating nonlinear transcranial ultrasound using a simplified head model.

© 2020 Author(s). All article content, except where otherwise noted, is licensed under a Creative Commons Attribution (CC BY) license (<http://creativecommons.org/licenses/by/4.0/>). <https://doi.org/10.1121/10.0002177>

(Received 14 May 2020; revised 17 September 2020; accepted 25 September 2020; published online 23 October 2020)

[Editor: Martin D. Verweij]

Pages: 2288–2300

### I. INTRODUCTION

Simulating the propagation of nonlinear acoustic waves is important for many branches of acoustics, including diagnostic ultrasound imaging, therapeutic ultrasound, underwater acoustics, and the study of sonic booms. Computationally, the key challenge is resolving the features of the nonlinear wave field while still remaining tractable to follow the evolution of the wave over many hundreds or thousands of wavelengths.<sup>1</sup> In the last decade, so called *full-wave* models have become popular. These directly solve the nonlinear wave equation (or the constitutive equations that are used to form it) and thereby inherently include the effects of nonlinear wave steepening, interaction with heterogeneous medium properties, and acoustic losses.<sup>2–7</sup>

Despite recent advances, for many problems that involve moderate or strong nonlinearity, full-wave modelling in three dimensions (3D) remains computationally challenging due to the very large grid sizes needed (often

$>1 \times 10^9$  grid points).<sup>1,8</sup> When the source geometry and the propagation medium are axisymmetric, the problem is reduced to two dimensions and the computational load is significantly reduced. This geometry is of practical interest, for example, in the study of nonlinear resonators<sup>9</sup> and modelling the output of therapeutic ultrasound transducers.<sup>10</sup> Previous full-wave models that consider nonlinear wave propagation in an axisymmetric coordinate system have been formulated using the finite difference time domain (FDTD) and finite element (FE) methods and used to solve the nonlinear Westervelt equation<sup>11,12</sup> or the corresponding constitutive equations.<sup>9,13–16</sup>

In the current work, the formulation, implementation, and validation of the axisymmetric wave model in the open-source  $k$ -Wave toolbox is described.<sup>17</sup> The model is based on the  $k$ -space pseudospectral time domain (PSTD) method as previously used to solve the nonlinear wave equation in a Cartesian coordinate system.<sup>5,18</sup> This formulation has advantages over FDTD and FE methods due to the reduced number of grid points needed per wavelength to reach convergence.<sup>19</sup> Fourier PSTD methods in an axisymmetric coordinate system have previously been used to solve the equations of linear acoustics,<sup>20</sup> Maxwell's equations,<sup>21,22</sup> and the equations of linear elasticity.<sup>23–26</sup> Here, the PSTD method is applied to solve the equations of nonlinear acoustics with two extensions: an approximate  $k$ -space correction

<sup>a)</sup>Portions of this work were presented in “Full-wave nonlinear ultrasound simulation in an axisymmetric coordinate system using the discrete sine and cosine transforms,” IEEE International Ultrasonics Symposium, Prague, Czech Republic, 21–25 July 2013.

<sup>b)</sup>Electronic mail: b.treeby@ucl.ac.uk, ORCID: 0000-0001-7782-011X.

<sup>c)</sup>ORCID: 0000-0002-4258-3262.

<sup>d)</sup>ORCID: 0000-0002-0087-8804.

<sup>e)</sup>ORCID: 0000-0001-7296-4093.

is used to improve the accuracy of the time integration, and discrete trigonometric transforms (DTTs) are used for gradient calculations in the radial direction to enforce the correct symmetry conditions in a computationally efficient manner.<sup>27</sup>

## II. MODEL FORMULATION

### A. Governing equations

The nonlinear propagation of acoustic waves through a medium with spatially varying acoustic properties and classical thermoviscous absorption can be described using a system of coupled partial differential equations<sup>5</sup>

$$\begin{aligned} \frac{\partial \mathbf{u}}{\partial t} &= -\frac{1}{\rho_0} \nabla p + \mathbf{F}, \\ \frac{\partial \rho}{\partial t} &= -(2\rho + \rho_0) \nabla \cdot \mathbf{u} - \mathbf{u} \cdot \nabla \rho_0 + M, \\ p &= c_0^2 \left( \rho + \mathbf{d} \cdot \nabla \rho_0 + \frac{B}{2A} \frac{\rho^2}{\rho_0} + 2\alpha_0 c_0 \frac{\partial \rho}{\partial t} \right). \end{aligned} \quad (1)$$

Here, the acoustic field is described by the pressure  $p$ , particle velocity  $\mathbf{u}$ , particle displacement  $\mathbf{d}$ , and acoustic density  $\rho$ , which vary as a function of position  $\mathbf{x}$  and time  $t$ . The propagation medium is described by the mass density  $\rho_0$ , sound speed  $c_0$ , nonlinearity parameter  $B/A$ , and absorption coefficient  $\alpha_0$ , all of which can vary as a function of position. For the parameter range of interest, the loss term in the pressure-density relation accounts for acoustic absorption of the form  $\alpha \approx \alpha_0 \omega^2$ , where  $\alpha_0$  is the absorption coefficient pre-factor given in units of Np (rad/s)<sup>-2</sup> m<sup>-1</sup>. Two linear source terms are also included, where  $\mathbf{F}$  is a force source term that represents the input of body forces per unit mass in units of N kg<sup>-1</sup> (or m s<sup>-2</sup>) and  $M$  is a mass source term that represents the time rate of the input of mass per unit volume in units of kg m<sup>-3</sup> s<sup>-1</sup>.<sup>1</sup> These equations can be combined to give a form of the Westervelt equation<sup>28</sup>

$$\begin{aligned} \nabla^2 p - \frac{1}{c_0^2} \frac{\partial^2 p}{\partial t^2} - \frac{1}{\rho_0} \nabla \rho_0 \nabla p + \frac{\beta}{\rho_0 c_0^4} \frac{\partial^2 p^2}{\partial t^2} + \frac{2\alpha_0}{c_0} \frac{\partial^3 p}{\partial t^3} \\ = \rho_0 \nabla \cdot \mathbf{F} - \frac{\partial M}{\partial t}, \end{aligned} \quad (2)$$

where  $\beta = 1 + B/2A$ .

If the wave field and propagation medium are axisymmetric such that there is no angular variation about an axis of symmetry, Eq. (1) can be rewritten in cylindrical coordinates where  $\mathbf{u} = u_x \hat{\mathbf{x}} + u_r \hat{\mathbf{r}}$  and the gradients with respect to the angular variable are zero (see Fig. 1). This gives the following expansions for the gradient, divergence, and Laplacian operators:

$$\begin{aligned} \nabla p &= \frac{\partial p}{\partial x} \hat{\mathbf{x}} + \frac{\partial p}{\partial r} \hat{\mathbf{r}}, \\ \nabla \cdot \mathbf{u} &= \frac{\partial u_x}{\partial x} + \frac{\partial u_r}{\partial r} + \frac{u_r}{r}, \\ \nabla^2 p &= \frac{\partial^2 p}{\partial x^2} + \frac{\partial^2 p}{\partial r^2} + \frac{1}{r} \frac{\partial p}{\partial r}, \end{aligned} \quad (3)$$

where  $\hat{\mathbf{x}}$  and  $\hat{\mathbf{r}}$  are unit vectors in the axial and radial directions, respectively. Using these expansions, Eq. (1) becomes

$$\begin{aligned} \frac{\partial \mathbf{u}}{\partial t} &= -\frac{1}{\rho_0} \left( \frac{\partial p}{\partial x} \hat{\mathbf{x}} + \frac{\partial p}{\partial r} \hat{\mathbf{r}} \right) + \mathbf{F}, \\ \frac{\partial \rho}{\partial t} &= -(2\rho + \rho_0) \left( \frac{\partial u_x}{\partial x} + \frac{\partial u_r}{\partial r} + \frac{u_r}{r} \right) + M, \\ p &= c_0^2 \left( \rho + \frac{B}{2A} \frac{\rho^2}{\rho_0} + 2\alpha_0 c_0 \frac{\partial \rho}{\partial t} \right), \end{aligned} \quad (4)$$

where the  $\mathbf{u} \cdot \nabla \rho_0$  and  $\mathbf{d} \cdot \nabla \rho_0$  terms in Eq. (1) are omitted as they cancel when these equations are solved.<sup>5</sup>

### B. Nonstandard PSTD method

To solve Eq. (4), a nonstandard or  $k$ -space PSTD method is used.<sup>19,29</sup> This approach uses the Fourier

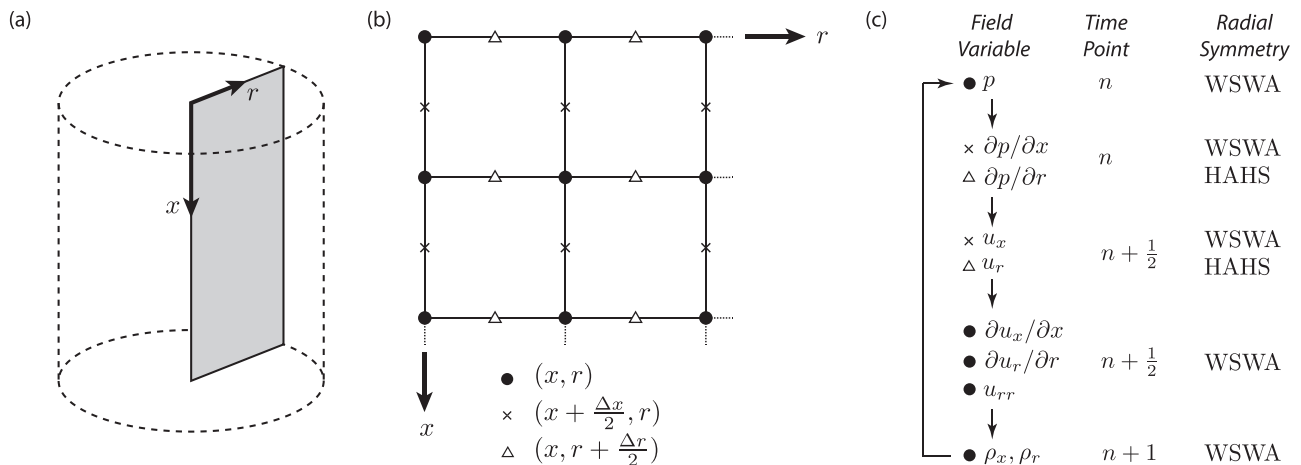


FIG. 1. (a) Axisymmetric coordinate system, where  $x$  is the axial coordinate and  $r$  is the radial coordinate. The dashed cylinder shows the angular symmetry. (b) Staggered grid formulation, where the radial particle velocity is calculated on a staggered grid in the radial direction (triangles), and the axial particle velocity is calculated on a staggered grid in the axial direction (crosses). (c) Summary of the update steps and corresponding radial symmetry.

collocation spectral method to calculate spatial gradients and a  $k$ -space corrected finite difference scheme to integrate in time, and can be considered as an extension to nonstandard finite difference methods.<sup>30</sup> The merits of this scheme have been discussed in detail elsewhere, e.g., Refs. 5, 18, 19, 29, and 31. In short, the scheme is exact and unconditionally stable in the limit of linear wave propagation in a homogeneous and lossless medium and can significantly reduce numerical dispersion compared to other methods for nonlinear wave propagation in heterogeneous and lossy media.

Here, the general formulation of the nonstandard PSTD method given in Ref. 32 is used to derive the  $k$ -space correction term for the wave equation in an axisymmetric coordinate system. Consider the linear and lossless wave equation for homogeneous media written in the following form:

$$\frac{\partial^2 p(x, r, t)}{\partial t^2} = Lp(x, r, t), \quad (5)$$

where  $L$  is a spatial differential operator given by

$$L = c_0^2 \left( \frac{\partial^2}{\partial x^2} + \frac{\partial^2}{\partial r^2} + \frac{1}{r} \frac{\partial}{\partial r} \right). \quad (6)$$

An exact time stepping scheme for Eq. (5) is given by<sup>32</sup>

$$\frac{p(x, r, t + \Delta t) - 2p(x, r, t) + p(x, r, t - \Delta t)}{\Delta t^2} = \mathcal{F}^{-1} \left\{ \kappa^2 \lambda \mathcal{F} \{ p(x, r, t) \} \right\}, \quad (7)$$

where  $\lambda$  is the Fourier representation of the differential operator  $L$ , and  $\kappa$  is the  $k$ -space correction term given by

$$\kappa = \text{sinc} \left( \sqrt{-\lambda} \Delta t / 2 \right), \quad (8)$$

where  $\text{sinc} = \sin(x)/x$ . The Fourier representation of  $L$  is given by

$$\lambda = c_0^2 \left( \frac{ik_r}{r} - k_r^2 - k_x^2 \right). \quad (9)$$

However, in this case,  $\lambda$  is a function of both  $k$  and  $r$  and, thus, cannot be directly applied in  $k$ -space (note, it is possible to apply mixed-domain  $k$ -space operators, e.g., Ref. 33, however, this is computationally expensive). An approximate  $k$ -space correction term can still be derived by considering that away from the radial origin, the contribution of the  $1/r$  term decreases, where

$$\lim_{r \rightarrow \infty} \lambda = -c_0^2 (k_r^2 + k_x^2), \quad (10)$$

which gives

$$\kappa \approx \text{sinc} \left( c_0 \sqrt{k_r^2 + k_x^2} \Delta t / 2 \right). \quad (11)$$

Equation (11) is the same as the exact  $k$ -space term used for the wave equation in Cartesian coordinates<sup>19</sup> and, here, is

exact for plane waves propagating in the  $\hat{x}$  direction and approximate for cylindrical waves propagating in the  $\hat{r}$  direction (with the accuracy increasing as  $r$  increases). While  $\kappa$  is derived using the second-order wave equation, it can also be applied when solving a system of coupled first-order equations as discussed in Refs. 29 and 31.

The  $k$ -space correction derived above accounts for numerical errors in the discretisation of the  $\partial^2 p / \partial t^2$  term using a finite difference scheme (or the equivalent first-order expressions). A similar correction is needed to account for the discretisation of the time varying source terms in Eq. (4) as discussed in Ref. 34. By again considering the limit as  $r \rightarrow \infty$ , the  $k$ -space source correction  $\sigma$  is given by

$$\sigma \approx \cos \left( c_0 \sqrt{k_r^2 + k_x^2} \Delta t / 2 \right). \quad (12)$$

Numerical experiments demonstrating the accuracy of the  $k$ -space correction terms are given in Sec. III.

### C. Spatial gradient calculation

In an axisymmetric coordinate system, the pressure field is symmetric about the axial coordinate axis (see Fig. 1). One approach to calculate spatial gradients in the radial direction is to mirror the field values about the origin to create the correct symmetry, and then use the Fourier collocation spectral method.<sup>21,23</sup> However, this doubles the size of the computational domain and, therefore, reduces the computational performance. An alternative approach is to use another basis to compute the spatial gradients that already imposes the required symmetry. In the current work, the Fourier basis normally used in the PSTD method is replaced with a sine or cosine basis.<sup>27</sup> In the discrete case, the basis function weights are calculated using the discrete cosine transform (DCT) and discrete sine transform (DST), collectively called the DTTs. In the axial direction, the standard Fourier collocation spectral method is used.

There are 16 DTTs (8 DCTs and 8 DSTs),<sup>35</sup> and the choice of transform depends on the symmetry at both ends of the computational domain in the radial dimension. Using the standard staggered grid formulation, the acoustic pressure is calculated at the radial origin, while the radial particle velocity is calculated on a staggered grid offset from the origin by half the grid point spacing.<sup>29</sup> The origin symmetry of the pressure  $p$  and the axial particle velocity  $u_x$  is WS (whole-sample symmetric), whereas the symmetry of the particle velocity in the radial direction  $u_r$  is HA (half-sample antisymmetric). At the outer boundary, a perfectly matched layer (PML) is used to absorb outgoing waves as described in Sec. IID. This means the outer radial boundary condition is not important and either symmetric or antisymmetric extensions can be chosen. In this case, a WA (whole-sample antisymmetric) extension is used for the acoustic pressure and axial particle velocity as this corresponds to DCT-III, which is more computationally efficient to compute than some of the other DTTs.<sup>36</sup> It also belongs to a transform group in which the representative samples have the same

length, making implementation easier.<sup>27</sup> The corresponding outer symmetry for the radial particle velocity is given by HS (half-sample symmetric).

Following Ref. 27, spectral gradient calculations can now be computed, including a shift to and from the spatially staggered grid. Assuming WSWA symmetry in the radial dimension, the spatial gradient of the pressure is given by

$$\begin{aligned} \frac{\partial p}{\partial x} &= C_3^{-1} \{ \mathcal{F}^{-1} \{ i k_x e^{i k_x \Delta x / 2} \mathcal{F} \{ C_3 \{ p \} \} \} \}, \\ \frac{\partial p}{\partial r} &= S_4^{-1} \{ \mathcal{F}^{-1} \{ -k_r \mathcal{F} \{ C_3 \{ p \} \} \} \}. \end{aligned} \tag{13}$$

Here,  $C_3$  is DCT-III and  $S_4$  is DST-IV (etc.) applied in the radial direction,  $\mathcal{F}$  is the Fourier transform applied in the axial direction,  $i = \sqrt{-1}$ ,  $\Delta x$  is the grid spacing in the axial direction, and  $k_x$  and  $k_r$  are the axial and radial wavenumbers, respectively (see Ref. 27 for definitions of the discrete wavenumber vectors). Similarly, assuming WSWA symmetry for the axial particle velocity and HAHS symmetry for the radial particle velocity, the corresponding spatial gradients are given by

$$\begin{aligned} \frac{\partial u_x}{\partial x} &= C_3^{-1} \{ \mathcal{F}^{-1} \{ i k_x e^{-i k_x \Delta x / 2} \mathcal{F} \{ C_3 \{ u_x \} \} \} \}, \\ \frac{\partial u_r}{\partial r} &= C_3^{-1} \{ \mathcal{F}^{-1} \{ k_r \mathcal{F} \{ S_4 \{ u_r \} \} \} \}. \end{aligned} \tag{14}$$

Note that due to the application of the  $k$ -space operator, the transformations to  $k$ -space are always calculated in two dimensions, not in one dimension as in the conventional PSTD method.<sup>29</sup> The Fourier transforms are always performed over the axial or  $x$ -dimension, and the DTTs are always performed over the radial or  $r$ -dimension. In the radial dimension, the grid shifting is implicit through the choice of DTT, so no additional shift term is required.<sup>27</sup> Note also that the spatial gradients in the radial direction could alternatively be computed using a Hankel transform.<sup>37</sup> However, currently there are no exact discrete Hankel transforms with equivalent computational performance to a fast Fourier transform (FFT) or DTT.

#### D. PML

To absorb the outgoing waves when they reach the edge of the computational domain, a split-field PML is used as derived in Ref. 29. The PML profile is given by

$$\text{PML} = e^{-\mu \Delta t / 2}, \quad \text{where } \mu = \frac{\phi c_0}{\Delta x} \left( \frac{m}{M} \right)^4. \tag{15}$$

Here,  $M$  is the size of the PML in grid points,  $m = 1, 2, 3, \dots, M$  is the index of the grid coordinate within the PML starting from the inner boundary, and  $\phi$  is the absorption coefficient within the PML given in units of Nepers per grid point. In the axial direction, the PML is applied at both ends of the domain. In the radial direction, the PML is only applied at the outer edge. On the staggered grid, the grid

index  $m$  is offset by 1/2. The performance of the PML is evaluated in Ref. 38 using the one-dimensional (1D) and two-dimensional (2D) Cartesian wave models in  $k$ -Wave, which use the same PML formulation.<sup>17</sup> For waves close to normal incidence, the reduction in wave amplitude is typically  $-80$  to  $-100$  dB, depending on the layer thickness and frequency of the incident wave.

#### E. Time stepping and model solution

To run the model, the acoustic field variables are updated in a time stepping fashion as detailed below. The superscripts  $n$  and  $n + 1$  indicate the field variables at the current and next time steps, respectively, and  $n - \frac{1}{2}$  and  $n + \frac{1}{2}$  indicate the field variables at the current and next time steps on the time staggered grid, respectively. A summary of the steps is given in Fig. 1(c). Implementation and benchmarking of the corresponding computer code are described in the Appendix.

- (1) Calculate the spatial gradients of the pressure field using a Fourier/DTT spectral collocation method as given in Eq. (13), including the application of the  $k$ -space correction  $\kappa$  given in Eq. (11)

$$\begin{aligned} \frac{\partial p^n}{\partial x} &= C_3^{-1} \{ \mathcal{F}^{-1} \{ i k_x e^{i k_x \Delta x / 2} \kappa \mathcal{F} \{ C_3 \{ p^n \} \} \} \}, \\ \frac{\partial p^n}{\partial r} &= S_4^{-1} \{ \mathcal{F}^{-1} \{ -k_r \kappa \mathcal{F} \{ C_3 \{ p^n \} \} \} \}. \end{aligned} \tag{16}$$

The individual transforms are applied in one dimension with DTTs applied in the radial dimension and FFTs applied in the axial dimension.

- (2) Update the particle velocity using a first-order forward difference with a step size of  $\Delta t$ , including application of a split-field PML

$$\begin{aligned} u_x^{n+1/2} &= \text{PML}_x \left( \text{PML}_x u_x^{n-1/2} - \frac{\Delta t}{\rho_0} \frac{\partial p^n}{\partial x} \right), \\ u_r^{n+1/2} &= \text{PML}_r \left( \text{PML}_r u_r^{n-1/2} - \frac{\Delta t}{\rho_0} \frac{\partial p^n}{\partial r} \right). \end{aligned} \tag{17}$$

The PML profile is defined in Eq. (15). Note, the temporal staggering between the pressure and particle velocity arises because the update steps are interleaved with the spatial gradient calculations.

- (3) Add force (velocity) source terms, including the  $k$ -space source correction  $\sigma$  given in Eq. (12),

$$\begin{aligned} u_x^{n+1/2} &= u_x^{n+1/2} + \Delta t C_3^{-1} \{ \mathcal{F}^{-1} \{ \sigma \mathcal{F} \{ C_3 \{ F_x^n \} \} \} \}, \\ u_r^{n+1/2} &= u_r^{n+1/2} + \Delta t S_4^{-1} \{ \mathcal{F}^{-1} \{ \sigma \mathcal{F} \{ S_4 \{ F_r^n \} \} \} \}. \end{aligned} \tag{18}$$

Here,  $\mathbf{F} = F_x \hat{\mathbf{x}} + F_r \hat{\mathbf{r}}$  and the source terms vary as a function of position and time. Without the  $k$ -space source correction, the transforms are not needed, and the source terms are added directly to the velocity field. Analogous to the gradient calculations, the DTTs used to transform to and from  $k$ -space in the radial direction

are chosen based on the radial symmetry, where WSWA → DCT-III and HAHS → DST-IV.

- (4) Calculate the spatial gradients of the particle velocity using a Fourier/DTT spectral method and calculate  $u_r/r$

$$\begin{aligned} \frac{\partial u_x^{n+1/2}}{\partial x} &= C_3^{-1} \left\{ \mathcal{F}^{-1} \left\{ ik_x e^{-ik_x \Delta x/2} \kappa \mathcal{F} \left\{ C_3 \left\{ u_x^{n+1/2} \right\} \right\} \right\} \right\}, \\ \frac{\partial u_r^{n+1/2}}{\partial r} &= C_3^{-1} \left\{ \mathcal{F}^{-1} \left\{ k_r \kappa \mathcal{F} \left\{ S_4 \left\{ u_r^{n+1/2} \right\} \right\} \right\} \right\}, \\ u_{rr}^{n+1/2} &= C_3^{-1} \left\{ \mathcal{F}^{-1} \left\{ \kappa \mathcal{F} \left\{ C_4 \left\{ u_r^{n+1/2}/r \right\} \right\} \right\} \right\}. \end{aligned} \quad (19)$$

Here,  $u_{rr} \equiv u_r/r$  after application of the  $k$ -space correction. Note, the symmetry of  $u_r$  changes from HAHS to HSHA after division by  $r$  (which is the radial position vector defined on the staggered grid), thus, DCT-IV is used as the forward transform for this term instead of DST-IV. The  $k$ -space correction term is applied to the entire right-hand side of the mass conservation equation given in Eq. (4), which includes both the spatial gradients and the  $u_r/r$  term. Computationally, the  $\partial u_r/\partial r$  and  $u_r/r$  terms are always used together, therefore, the inverse transforms can be combined.

- (5) Update the acoustic density using a first-order forward difference with a step size of  $\Delta t$ , including application of a split-field PML,

$$\begin{aligned} \rho_x^{n+1} &= \text{PML}_x \left( \text{PML}_x \rho_x^n - \Delta t (2\rho^n + \rho_0) \frac{\partial u_x^{n+1/2}}{\partial x} \right), \\ \rho_r^{n+1} &= \text{PML}_r \left( \text{PML}_x \rho_r^n - \Delta t (2\rho^n + \rho_0) \right. \\ &\quad \left. \times \left( \frac{\partial u_r^{n+1/2}}{\partial r} + u_{rr}^{n+1/2} \right) \right). \end{aligned} \quad (20)$$

Here,  $\rho^n = \rho_x^n + \rho_r^n$ , and the PML profile is defined in Eq. (15).

- (6) Add the mass source term, including a  $k$ -space source correction,

$$\begin{aligned} \hat{M} &= C_3^{-1} \left\{ \mathcal{F}^{-1} \left\{ \sigma \mathcal{F} \left\{ C_3 \left\{ M^n \right\} \right\} \right\} \right\}, \\ \rho_x^{n+1} &= \rho_x^{n+1} + \Delta t \hat{M} / 2, \\ \rho_r^{n+1} &= \rho_r^{n+1} + \Delta t \hat{M} / 2. \end{aligned} \quad (21)$$

Here,  $\hat{M}$  is the mass source after applying the source correction, and the source is divided evenly between the split field components of the density.

- (7) Update the acoustic pressure using the pressure-density relation

$$\begin{aligned} p^{n+1} &= c_0^2 \left( \rho^{n+1} + \frac{B}{2A} \frac{(\rho^{n+1})^2}{\rho_0} - \alpha_0 c_0 \rho_0 \left( \frac{\partial u_x^{n+1/2}}{\partial x} \right. \right. \\ &\quad \left. \left. + \frac{\partial u_r^{n+1/2}}{\partial r} + u_{rr}^{n+1/2} \right) \right), \end{aligned} \quad (22)$$

where  $\rho^{n+1} = \rho_x^{n+1} + \rho_r^{n+1}$ . To avoid needing to calculate the temporal derivative of the density, the  $\partial \rho / \partial t$  term is replaced here using the linearised version of the conservation of mass given in Eq. (4). Under the assumption that the absorption has a second-order effect on the wave field, the substitution of first-order terms into second-order terms leads to third-order errors, which can be neglected.

Note, the use of a spatially and temporally staggered grid means care must be taken when defining sources and extracting outputs from the model. In particular, the discrete values of the particle velocity are calculated on a grid offset by  $\Delta x/2$  and  $\Delta t/2$  relative to the acoustic pressure. Additionally, there is an offset of  $\Delta t/2$  between the inputs and outputs, i.e., between the force source term and the calculated particle velocity and the mass source term and the calculated density and pressure.

### III. NUMERICAL EXPERIMENTS

#### A. Nonlinearity and absorption for a plane wave

To demonstrate the performance and capabilities of the developed model, a series of numerical experiments was performed. First, to simulate the propagation of a plane wave in the axial direction, the radial symmetry at the outer edge of the domain was modified to be symmetric (i.e., WSWA) and the PML was disabled in the radial dimension. In this case, simulations compared with the 1D  $k$ -space code in  $k$ -Wave agreed to machine precision (with normalised maximum errors of  $< 1 \times 10^{-14}$ ).

For the linear propagation of an axial plane wave in a homogeneous and lossless medium, the model is exact and unconditionally stable.<sup>29</sup> When the medium is absorbing, the model is no longer exact, but still highly accurate. Figure 2 shows results from a numerical example of a 1D plane wave propagating through a lossy medium with different absorption coefficients. In this example, the propagation of a broadband pulse (defined as a discrete spatial delta function filtered using a Blackman window<sup>39</sup>) was recorded at two sensor positions spaced 1 mm apart. The grid size was defined using 1024 axial grid points, with  $\Delta x = 7.5 \mu\text{m}$ ,  $c_0 = 1500 \text{ m s}^{-1}$ , and  $\Delta t = 0.25 \text{ ns}$  (the radial dimension does not affect the simulation for an axial plane wave). The frequency dependent absorption was then calculated from the amplitude spectra of the two recorded signals.

The open circles in Fig. 2 correspond to the simulation results using a Courant-Friedrichs-Lewy (CFL) number of  $\text{CFL} = c_0 \Delta t / \Delta x = 0.05$ . There is very close agreement between the model and the corresponding analytical power law across the full simulation bandwidth (up to the Nyquist limit of 100 MHz), including at very high absorption values up to 500 dB/cm. As the CFL is increased, the accuracy decreases slightly due to errors in the calculation of  $\partial \rho / \partial t$  using the linearised mass conservation equation. This is because the velocity gradient values are offset from the acoustic density values by  $\Delta t/2$ . The corresponding results for a CFL of 0.3 are shown with the filled dots in Fig. 2.

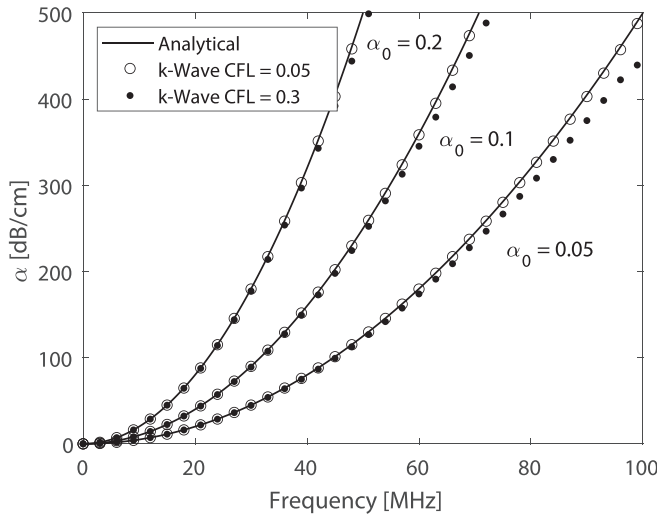


FIG. 2. Frequency dependent acoustic absorption calculated for a plane wave in a lossy medium compared to the analytical values for different values of the absorption coefficient  $\alpha_0$  given in units of  $\text{dB MHz}^{-2} \text{cm}^{-1}$ . The open circles correspond to model results for a CFL number of 0.05, and the filled dots correspond to model results for a CFL of 0.3.

However, even in this case, the numerical results are still accurate up to approximately half the simulation bandwidth or 4 grid points per wavelength (PPW), which is sufficient for most practical applications.

In a second numerical experiment, the nonlinear propagation of a harmonic plane wave through an absorbing medium was simulated for different values of the shock parameter and Gol'dberg number (see, e.g., Ref. 47 for definitions) as shown in Fig. 3. In this case, a 20 MPa 1 MHz continuous wave source was propagated for 20 wavelengths and the recorded sensor data compared with the series solution given by Mendousse.<sup>28</sup> The grid size was defined using 4374 axial grid points, with  $\Delta x = 7.5 \mu\text{m}$ ,  $c_0 = 1500 \text{ m s}^{-1}$ ,  $\rho_0 = 1000 \text{ kg m}^{-3}$ , and  $\Delta t = 0.5 \text{ ns}$ . This gave a Nyquist limit of 100 MHz, meaning the model captured the first 100 harmonics of the source frequency. Uniform values for  $B/A$  and  $\alpha_0$  were set based on the values for the shock parameter and Gol'dberg number, respectively. There is close quantitative agreement between the model and reference solution with the maximum error in the spectral amplitudes in all cases less than 0.2%.

### B. Accuracy of the $k$ -space correction

For linear wave propagation in homogeneous and lossless media, the  $k$ -space correction used as part of the finite difference time integration scheme is exact for plane waves travelling in the axial direction but only approximate for cylindrical waves travelling in the radial direction (see Sec. II B). To examine the accuracy of this approximation in practice, the propagation of a broadband cylindrical wave pulse was simulated. The source position was moved along the radial axis, and the source-to-sensor distance was kept fixed at 50 mm. The grid size was defined using 128 radial grid points with  $\Delta r = 1 \text{ mm}$ ,  $c_0 = 1500 \text{ m s}^{-1}$ , and  $\Delta t = 33.3 \text{ ns}$  (giving a

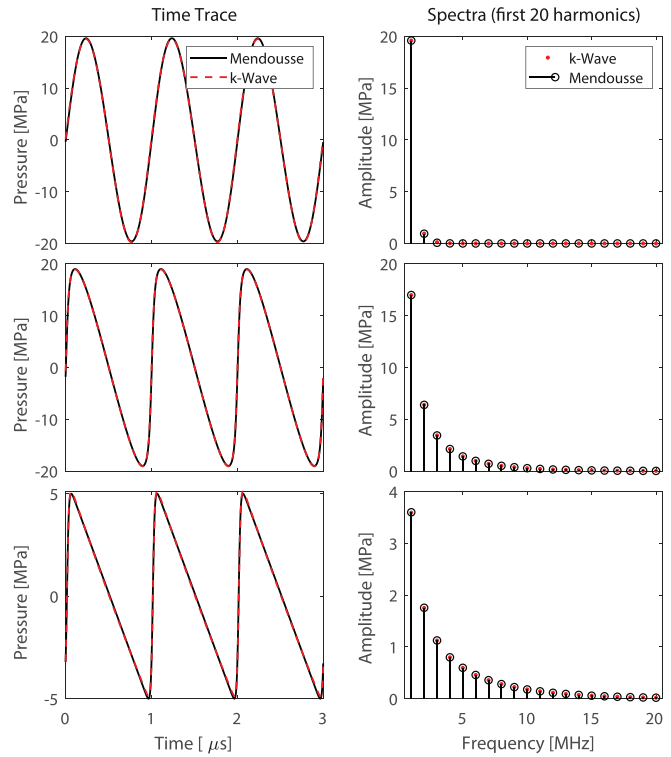


FIG. 3. (Color online) Recorded time series and corresponding amplitude spectra after propagating a nonlinear plane wave through an absorbing medium for different values of the shock parameter  $\sigma_{\text{sh}}$  and Gol'dberg number  $\Gamma$ . (Top)  $\sigma_{\text{sh}} = 0.1$  and  $\Gamma = 5$ , (middle)  $\sigma_{\text{sh}} = 1$  and  $\Gamma = 20$ , (bottom)  $\sigma_{\text{sh}} = 10$  and  $\Gamma = 50$ .

CFL of 0.5). In the axial direction, the PML was disabled and the source replicated to allow the simulation of an infinite cylindrical wave. The simulations were repeated with and without the  $k$ -space correction and with the time step reduced by a factor of 2 and a factor of 500 for reference.

The error as a function of the source position and CFL and an example of the recorded waveforms are shown in Fig. 4. Although the  $k$ -space correction in the radial direction is only approximate, in practice, it significantly reduces the dispersion error. There is a small increase in the error when the source is placed at the origin, but otherwise the error is relatively constant with the source distance as shown in Fig. 4(b). Both with and without the  $k$ -space correction, the simulation converges (the error reduces) as the time step is reduced. The error convergence with the time step size is shown in Fig. 4(c). For this simulation, when the  $k$ -space correction is included, a CFL of 0.26 is required to reduce the maximum error to less than 1%, and a CFL of 0.08 is required to reduce the error below 0.1%. Without the  $k$ -space correction, a CFL of 0.05 is required to reduce the error to less than 1%, which corresponds to a fivefold increase in the number of time steps required.

A cylindrical wave corresponds to an infinite line source in three dimensions. In a 2D Cartesian coordinate system, this can be simulated using a point source. However, simulations of a cylindrical wave using the 2D and axisymmetric models in  $k$ -Wave do not agree to machine precision in the same way as the simulation of a

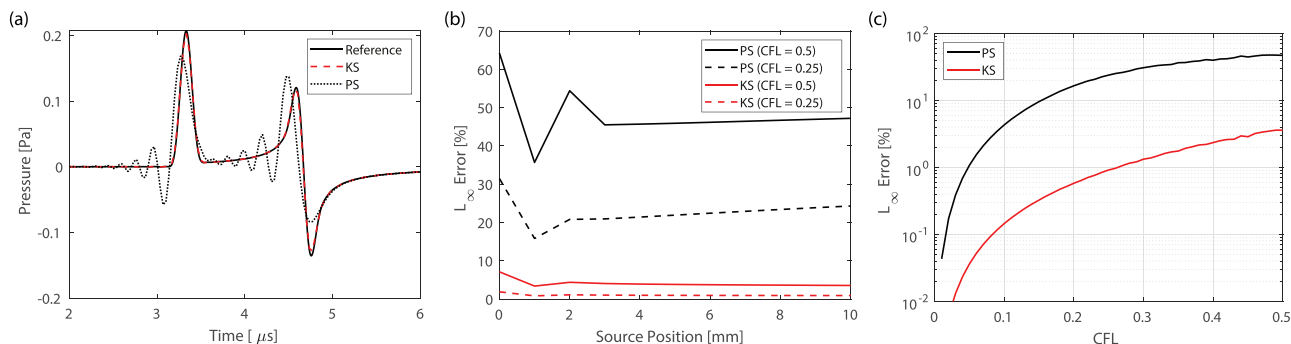


FIG. 4. (Color online) Accuracy of the  $k$ -space correction for a cylindrical wave. (a) Example of the recorded pressure signals when the source is 5 mm from the radial origin (the source pressure is 1 Pa). The reference simulation is calculated using a CFL of 0.001 and compared with the  $k$ -space corrected (KS) and conventional pseudospectral (PS) models using a CFL of 0.5. (b)  $L_\infty$  error (maximum difference between the two signals normalised by the maximum of the reference signal) as a function of the source position relative to the radial origin for CFL numbers of 0.5 and 0.25. (c)  $L_\infty$  error as a function of the CFL number for a source position of 5 mm.

1D plane wave does. This is because the discretisation of the wavenumber domain in the 2D Cartesian code is square, thus, the band-limited interpolant is not rotationally symmetric. For simulations in which the bandwidth is restricted (i.e., using a Gaussian shaped source), there is very close agreement between the two models when a small time step is used (maximum error  $< 0.1\%$ ). For larger time steps, provided the source shape is not staircased, the 2D Cartesian code is more accurate as the  $k$ -space correction has the same accuracy for waves propagating in all directions.

### C. Modelling piston and bowl sources

A common application for axisymmetric wave models is the simulation of plane piston and focused bowl acoustic sources. These transducers are widely used, for example, in non-destructive testing, ultrasound metrology, and ultrasound therapy. To demonstrate the accuracy of the developed model in this case, two transducers were simulated and compared to analytical results.

First, the acoustic field generated by a plane piston transducer with a diameter of 10 mm driven by a continuous wave 1 MHz sinusoid was simulated in a homogeneous and lossless medium. The source was defined with the staircase-free formulation described in Ref. 40, using the exact band-limited interpolant and an upsampling rate of 100. The domain size was set to 40 mm in the axial direction and 20 mm in the radial dimension with  $c_0 = 1500 \text{ m s}^{-1}$  and  $\rho_0 = 1000 \text{ kg m}^{-3}$ . The grid step and time step were defined using a variable number of PPW from 3 to 6 and CFL numbers from 0.025 to 0.5. The simulations were repeated with and without the  $k$ -space source correction term  $\sigma$  (the  $k$ -space correction for the time integration  $\kappa$  was always used). The simulation results were compared with the analytical solution for the axial pressure from a piston transducer given in Ref. 41.

An example of the amplitude of the simulated pressure field in steady state using 5 PPW and a CFL of 0.15 is shown in Fig. 5(a), with a comparison against the analytical solution shown in Fig. 5(b). (Note, for display, the pressure field is always mirrored in the radial dimension.) The error as a function of the CFL number for different PPW both

with (solid lines) and without (dashed lines) the  $k$ -space source correction is shown in Fig. 5(c). At 4 PPW, a CFL of 0.275 is sufficient to reduce the error to 1%. Without the source correction, the error is increased by a factor of 3, and a CFL of 0.15 is required to reduce the error to 1%. At higher PPW, the CFL required to achieve a certain accuracy is relaxed, as the same CFL number corresponds to an increased number of points per period (PPP), where  $\text{CFL} = \text{PPW} / \text{PPP}$ . For this example, the  $k$ -space correction is exact for the plane wave component of the field, whereas it is only approximate for the toroidal edge wave that interacts to form the complex pattern of near-field interference.

Next, the acoustic field generated by a focused bowl transducer with a radius of curvature and aperture diameter of 30 mm driven by a continuous wave 1 MHz sinusoid was simulated in a homogeneous and lossless medium. The source was again defined with the staircase-free formulation described in Ref. 40, using the approximate band-limited interpolant with a truncation threshold of  $\epsilon = 1\%$  and an upsampling rate of 100. The domain size was set to 45 mm in the axial direction and 27.5 mm in the radial dimension. The simulations were repeated with the same parameters as the plane piston transducer and compared with the analytical solution for the axial pressure given in Ref. 42.

An example of the amplitude of the simulated pressure field in steady state using 5 PPW and a CFL of 0.15 is shown in Fig. 6(a) with a comparison against the analytical solution shown in Fig. 6(b). The error as a function of the CFL number is shown in Fig. 6(c). The accuracy of the focused bowl simulation is similar to the plane piston results. However, in this case, there is an error floor that is reached as the CFL is decreased. This is due to approximations made in the definition of the source geometry as discussed in Ref. 40 and related to the choice of the truncation threshold and upsampling rates.

### D. Scattering of plane wave by a fluid sphere

One of the advantages of a full-wave model is that it can account for multiple scattering from medium heterogeneities. For the case of a plane wave propagating through a layered medium, the accuracy of the axisymmetric model is



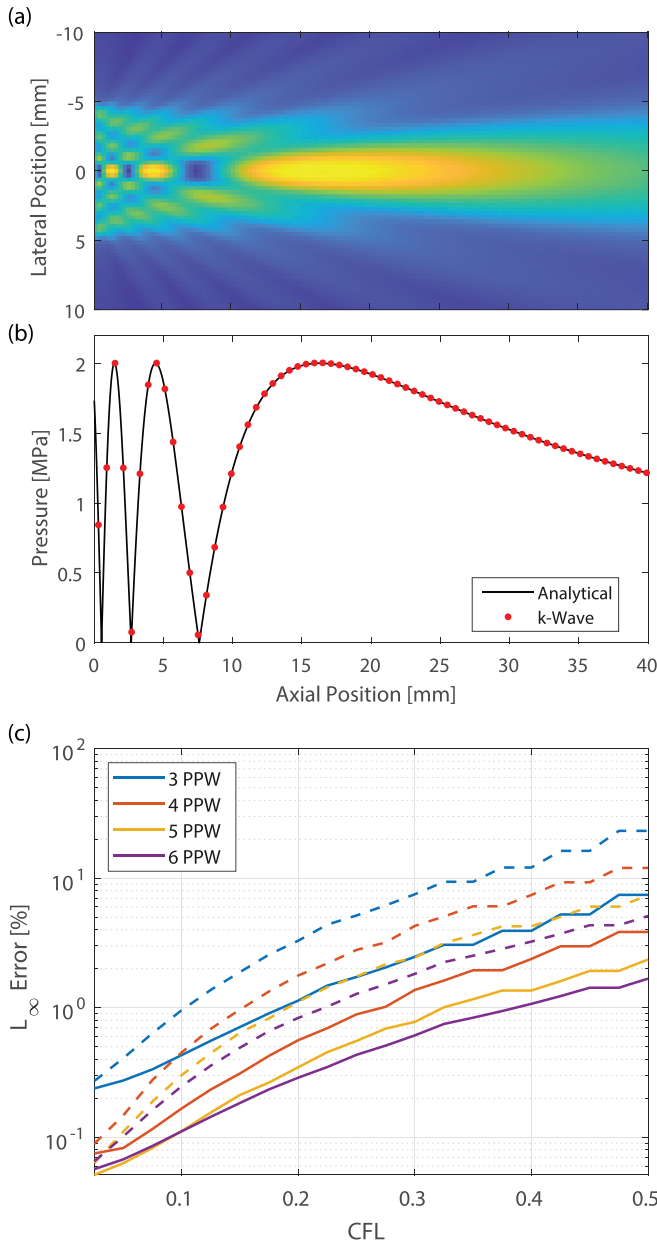


FIG. 5. (Color online) Simulation of the steady state pressure field from a plane piston transducer. (a) Simulated pressure amplitude using 5 PPW and a CFL number of 0.15. (b) Comparison of the axial pressure against the analytical solution. (c) Error in the axial pressure as a function of the CFL for different PPW both with (solid lines) and without (dashed lines) the *k*-space source correction.

identical to that reported in Refs. 5 and 38. To examine the accuracy of the model in the more general case, the scattering of an axial plane wave by a fluid sphere was simulated. This is a challenging problem for simulations based on structured grids as the complex diffraction pattern depends on the modes generated within the perfectly smooth sphere, whereas in the numerical model the representation of the sphere is staircased, particularly at low PPW.

Figure 7(a) shows the simulated pressure amplitude for the scattering of a 1 MHz monochromatic plane wave by a sphere of radius 2.5 mm. The medium properties were set to  $c_0 = 1500 \text{ m s}^{-1}$ ,  $\rho_0 = 1000 \text{ kg m}^{-3}$ ,  $c_{\text{sphere}} = 1700 \text{ m s}^{-1}$ ,

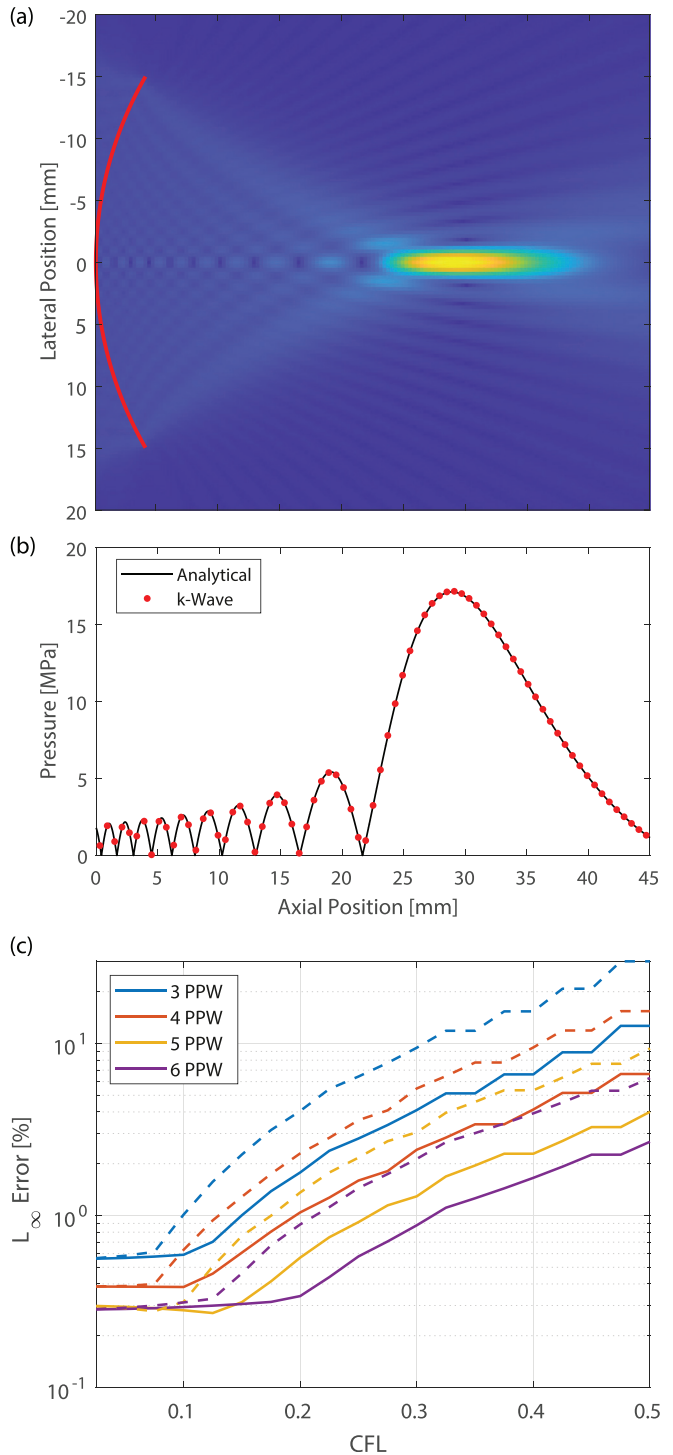


FIG. 6. (Color online) Simulation of the steady state pressure field from a focused bowl transducer. (a) Simulated pressure amplitude using 5 PPW and a CFL number of 0.15. (b) Comparison of the axial pressure against the analytical solution. (c) Error in the axial pressure as a function of the CFL for different PPW both with (solid lines) and without (dashed lines) the *k*-space source correction.

and  $\rho_{\text{sphere}} = 1100 \text{ kg m}^{-3}$ . The analytical solution given by Ref. 43 is also shown for comparison. There is good agreement between the two simulations; however, the convergence is slow compared to the other numerical experiments as shown in Fig. 7(c). In this case, to reduce the *L*<sub>2</sub> error to

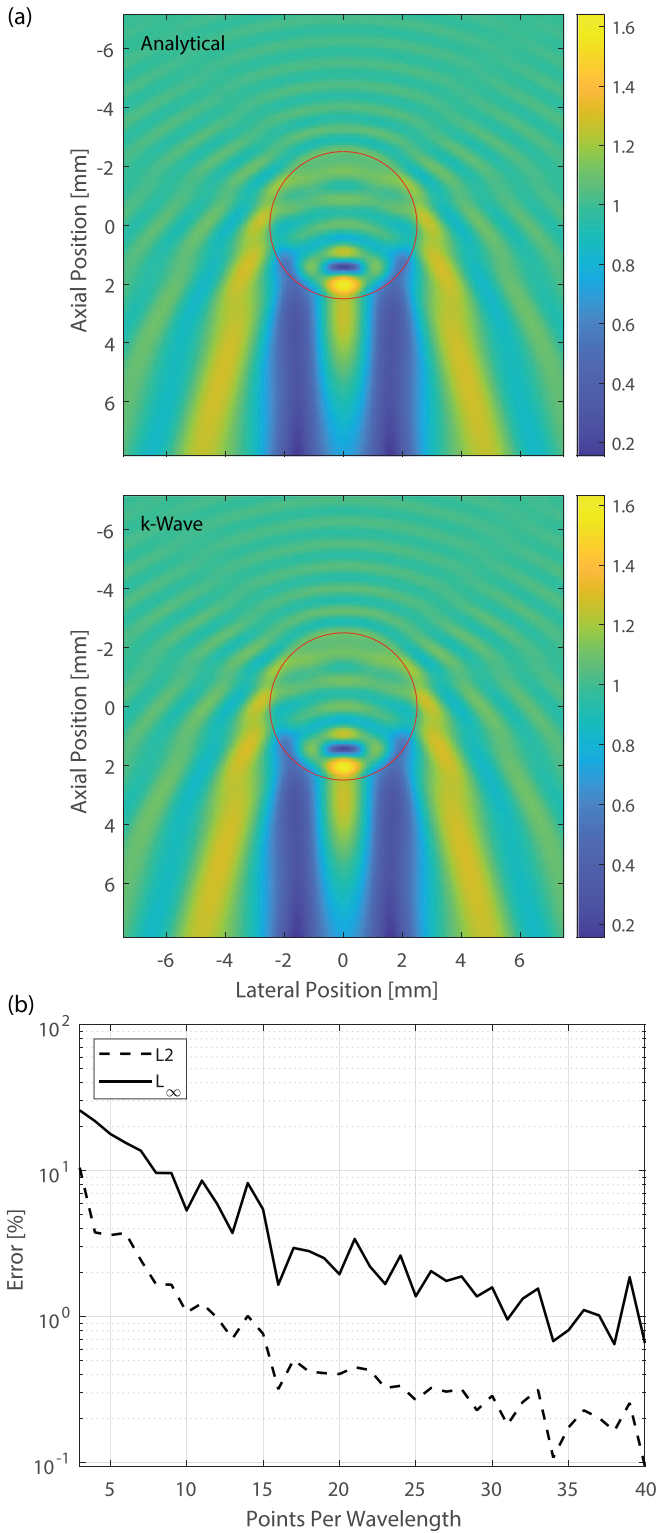


FIG. 7. (Color online) (a) Scattering of a monochromatic plane wave by a fluid sphere calculated using an analytical series solution and the axisymmetric model in *k*-Wave using 20 PPW. (b) Error as a function of PPW.

<1% requires >10 PPW. This is consistent with the numerical experiments performed in Refs. 38 and 44, which demonstrate that staircasing can be a significant source of numerical error for simulations on a regular Cartesian grid (for both FDTD and PSTD methods).

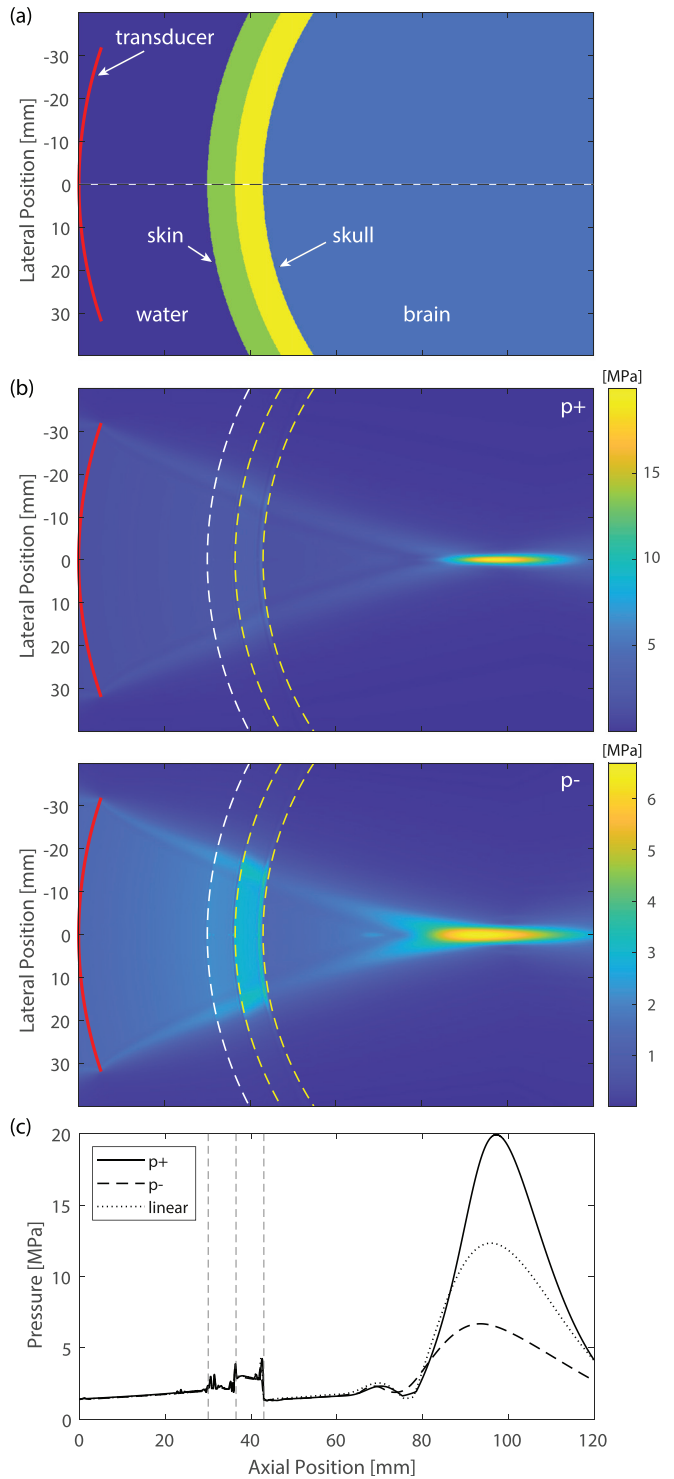


FIG. 8. (Color online) (a) Layout for a transcranial ultrasound simulation. (b) Temporal peak positive and negative pressure over the simulation duration. The dashed lines show the position of the medium interfaces. (c) Axial profile for the peak positive and negative pressure, along with the corresponding linear simulation for reference.

### E. Transcranial ultrasound simulation

The previous examples demonstrate the accuracy of the developed model in a number of cases in which analytical solutions are available. As a final example to demonstrate the utility of the model more generally, the nonlinear

TABLE I. Material properties used for the transcranial simulation.

	$c_0$ (m s <sup>-1</sup> )	$\rho_0$ (kg m <sup>-3</sup> )	$B/A$	$\alpha_0$ (dB MHz <sup>-2</sup> cm <sup>-1</sup> )
Water	1490	998	5.0	0.0025
Skin	1620	1110	6.7	1.5
Skull bone	2820	1730	370	2.2
Brain	1550	1050	6.7	0.55

propagation of ultrasound waves through an idealised human skull was simulated. The transducer was based on the nominal parameters of the Sonic Concepts H-151 focused bowl transducer (Sonic Concepts, Bothell, WA), which has an aperture diameter of 64 mm, radius of curvature of 100 mm, and centre frequency of 1.1 MHz. The transducer was driven by a Gaussian-windowed four cycle burst with a magnitude of 1.5 MPa. The medium geometry was defined using a simplified head geometry with four curved layers as shown in Fig. 8(a). The skull radius of curvature was set to 80 mm, the skull thickness was 6.5 mm, and the skin thickness was 6.5 mm. The material properties for each layer are given in Table I (these are based on representative values used in the literature).

The simulation domain size was 120 mm (axial) × 40 mm (radial) with  $\Delta x = \Delta r = 27 \mu\text{m}$  to give 50 PPW at the driving frequency (i.e., modelling up to the 25th harmonic). The resulting grid size was 4536 × 1536 grid points. The simulation was run for 100  $\mu\text{s}$  with a CFL of 0.1, giving  $\Delta t = 0.91$  ns with 110k time steps. The simulation was performed using the CL1 machine from Table II. The total simulation time was 49 min and consumed 900 MB of memory.

The peak positive and peak negative pressures over the simulation duration are displayed in Fig. 8(b) with the axial profile shown in Fig. 8(c), along with the results from a linear simulation for comparison. The peak positive and negative pressure become asymmetric due to the nonlinear propagation of the wave with a shift in the positions of the spatial peak positive and negative pressures compared to the linear case. In the region of the skull, the peak positive and negative pressures are similar to the linear case as discussed in Ref. 8.

The time signal recorded at the position of the spatial peak positive pressure is shown in Fig. 9, along with the corresponding amplitude spectrum. The pulse is distorted by nonlinear wave propagation. The echoes following the main pulse are due to round trip reflections within the skull. Only

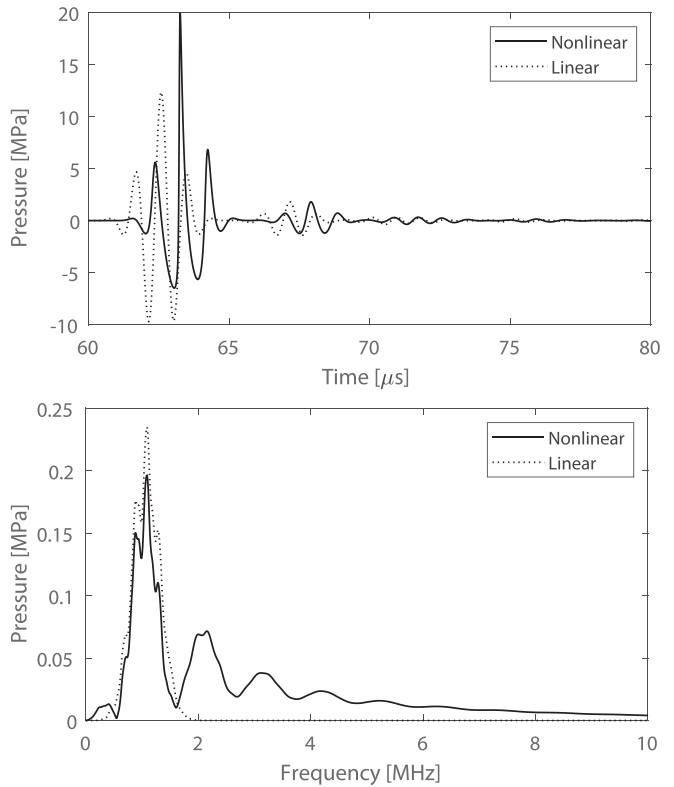


FIG. 9. Time domain pressure signal recorded at the position of spatial peak pressure for the transcranial simulation shown in Fig. 8, along with the corresponding amplitude spectrum.

a small number are discernible, which is consistent with recent simulation results using iterative one-way methods, which show that only a small number of reflections need to be considered.<sup>45</sup>

#### IV. SUMMARY

A full-wave ultrasound model, which accounts for nonlinear wave propagation in a heterogeneous and absorbing medium, is developed in an axisymmetric coordinate system. The governing equations are solved using a nonstandard or  $k$ -space PSTD method in which spatial gradients in the axial direction are calculated using the Fourier collocation spectral method, and spatial gradients in the radial direction are calculated using DTTs. The assumption of axisymmetry allows simulations with dense computational grids to model the propagation of nonlinear fields over large domains. The accuracy of the model is evaluated by

TABLE II. Hardware parameters of machines used for benchmarking experiments. “Cache” refers to the last-level cache size per processor. DDR: double data rate.

Reference	Cores	Processor name	Architecture	Launch	Cache	Instruction set	Memory
IB1	1 × 4	Intel i7-3770 at 3.9 GHz	Ivy Bridge	Q2/2012	8 MB	AVX	32 GB DDR3 1600 MHz
H1	2 × 6	Intel E5-2620v3 at 2.4 GHz	Haswell	Q3/2014	15 MB	AVX2	64 GB DDR3 2133 MHz
S1	2 × 8	Intel Xeon Silver 4110 at 2.1 GHz	Skylake	Q3/2017	11 MB	AVX-512	128 GB DDR4 2666 MHz
SB1	2 × 8	Intel E5-2665 at 2.4 GHz	Sandy Bridge	Q1/2012	20 MB	AVX	64 GB DDR 2133 MHz
H2	2 × 12	Intel E5-2680v3 at 2.5 GHz	Haswell	Q3/2014	30 MB	AVX2	128 GB DDR 2133 MHz
CL1	2 × 18	Intel Xeon Gold 6240 at 2.6 GHz	Cascade Lake	Q2/2019	25 MB	AVX-512	192 GB DDR4 2933 MHz

comparing with analytical solutions for linear and nonlinear plane waves in absorbing media, plane-piston and bowl-shaped transducers, and the scattering of a plane wave by a fluid sphere. Finally, the utility of the model is demonstrated by the simulation of nonlinear wave propagation through a simplified skull model. Both MATLAB and C++ versions of the axisymmetric model can be downloaded as part of the open-source *k*-Wave toolbox, available online.<sup>46</sup>

**ACKNOWLEDGMENTS**

This work was supported by the Engineering and Physical Sciences Research Council, United Kingdom. This work was also supported by The Ministry of Education, Youth and Sports from the National Programme of Sustainability (NPU II) project IT4Innovations excellence in science, Grant No. LQ1602, and the IT4Innovations infrastructure, which is supported by the Large Infrastructures for Research, Experimental Development and Innovations project IT4Innovations National Supercomputing Center, Grant No. LM2015070.

**APPENDIX: COMPUTER CODE AND PERFORMANCE BENCHMARKS**

The developed axisymmetric model was implemented using the C++ programming language. The code was designed for execution on a single shared-memory computer with calculations and data storage performed in single precision. DTTs and FFTs were computed using the FFTW library, and input and output files stored in hierarchical data format (HDF5). All computational kernels performing element-wise operations were parallelised and vectorised using OpenMP 4.0 and manually tuned to improve cache locality and reduce code branching. The creation of input files and the visualisation of output files was performed using MATLAB (The MathWorks, Natick, MA).

In the most general case (nonlinear simulation with all medium properties heterogeneous), 17 matrices are used within the simulation core and the memory usage can be estimated by

$$\text{memory usage (MB)} \approx \frac{17N_x N_r}{1024^2/4}, \tag{A1}$$

where  $N_x$  and  $N_r$  are the number of grid points in the axial and radial dimensions, respectively. Additional memory is also used to store the source terms and any aggregated output quantities (e.g., maximum pressure).

The performance of the code was investigated on a range of machines covering desktop computers and servers of different sizes and ages as outlined in Table II. For the benchmark simulations, the code was recompiled using the most appropriate instruction set for each machine using GCC 7.3 (Free Software Foundation, Inc.). The compute times per time step using all processor cores for grid sizes ranging from  $128^2$  to  $32768^2$  are shown in Fig. 10(a). For

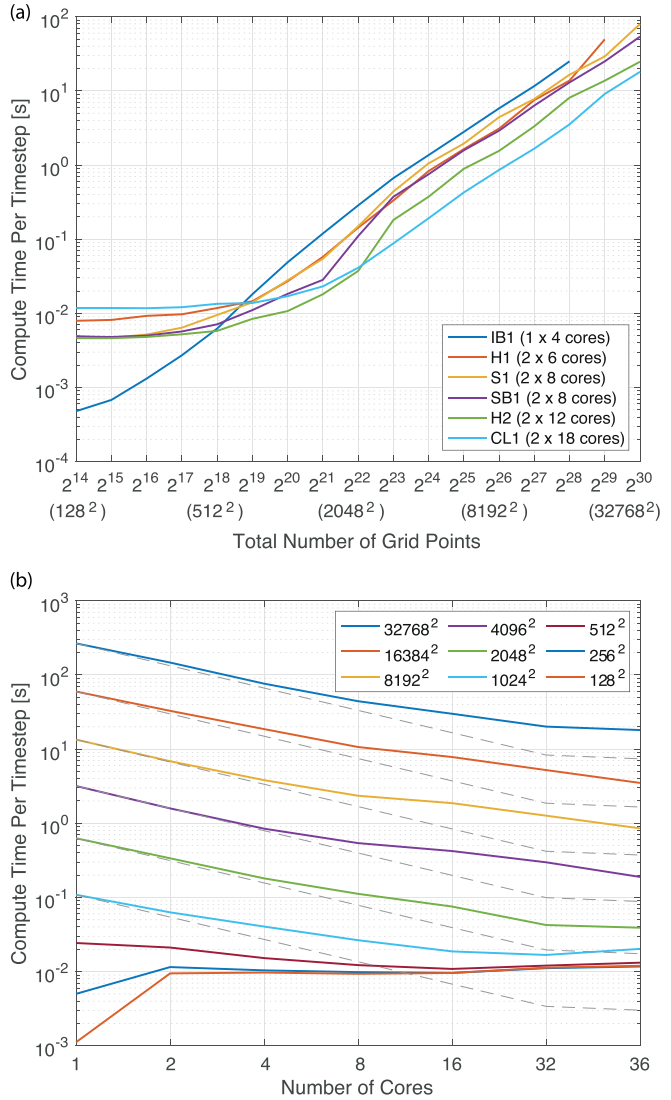


FIG. 10. (Color online) (a) Computational time per time step for different grid sizes for the machines given in in Table II. (b) Strong scaling performance using the CL1 machine in Table II, showing the computational time per time step for different dimension sizes and numbers of cores. The ideal strong scaling for each grid size is shown with a dashed grey line.

comparison, the strong scaling performance of the code using the CL1 machine is shown in Fig. 10(b). In this case, for each domain size, the number of computational threads was increased from 1 to 36 in powers of two.

For larger dimension sizes (above  $1024^2$ ), the code exhibits excellent weak scaling as seen in Fig. 10(a) with the execution time growing by a factor between 1.9 and 2.2 when the domain size is doubled. The differences between the various machines are dependent on a combination of the core count, instruction set, clock frequency, and bandwidth of the memory subsystem (in some cases, the clock frequency is automatically decreased if the advanced vector extension (AVX) instruction set AVX-512 is used).

In contrast, the strong scaling performance is less than ideal as seen in Fig. 10(b). The maximum speedup using 36 cores compared to 1 core is 15–17, giving a parallel efficiency of 42%–47%. There are two primary causes of this

behaviour. First, the calculations for larger grid sizes are memory bound due to the FFT transpositions and the low arithmetic intensity of the element-wise kernels. This means the memory bandwidth ultimately limits the performance. Second, the CL1 machine used for this benchmark uses dynamic frequency scaling, which reduces the maximum clock frequency as more cores are utilised (by 35% in the worst case). If the central processing unit (CPU) is instead used at a fixed frequency of 2.4 GHz, the speedup and efficiency increase from 21 to 24 and 59% to 66%, respectively.

For small dimension sizes (below  $512^2$ ), the performance of the code shown in Fig. 10(a) is almost constant. In this case, the memory used by the simulation core is small enough to fit within the L2 cache and, therefore, using multiple cores is counterproductive because of the additional communication overhead. This can be seen in Fig. 10(b), where for small dimension sizes, the compute time actually increases if more than a single core is used. Note, the IB1 machine is fastest for very small dimension sizes as it has only four cores and a very high clock frequency [almost 4 GHz when the Intel Turbo (Intel Corporation, Santa Clara, CA) is enabled].

For reference, compared to the MATLAB implementation of the axisymmetric model (using a FFTW implementation of the DTT<sup>27</sup>), the C++ code is on the order of 4–5 times faster for larger domain sizes (above  $1024^2$ ). For small domain sizes (below  $512^2$ ), the C++ code using a single core can be more than ten times faster due to improved cache locality, reuse of FFT execution plans, and other single instruction, multiple data (SIMD) optimisations.

<sup>1</sup>J. Jaros, A. P. Rendell, and B. E. Treeby, “Full-wave nonlinear ultrasound simulation on distributed clusters with applications in high-intensity focused ultrasound,” *Int. J. High Perf. Comput. Appl.* **30**(2), 137–155 (2016).

<sup>2</sup>C. W. Connor and K. Hynynen, “Bio-acoustic thermal lensing and nonlinear propagation in focused ultrasound surgery using large focal spots: A parametric study,” *Phys. Med. Biol.* **47**(11), 1911–1928 (2002).

<sup>3</sup>G. F. Pinton, J. Dahl, S. Rosenzweig, and G. E. Trahey, “A heterogeneous nonlinear attenuating full-wave model of ultrasound,” *IEEE Trans. Ultrason. Ferroelectr.* **56**(3), 474–488 (2009).

<sup>4</sup>K. Okita, K. Ono, S. Takagi, and Y. Matsumoto, “Development of high intensity focused ultrasound simulator for large-scale computing,” *Int. J. Numer. Meth. Fl.* **65**(1–3), 43–66 (2011).

<sup>5</sup>B. E. Treeby, J. Jaros, A. P. Rendell, and B. Cox, “Modeling nonlinear ultrasound propagation in heterogeneous media with power law absorption using a  $k$ -space pseudospectral method,” *J. Acoust. Soc. Am.* **131**(6), 4324–4336 (2012).

<sup>6</sup>L. Demi, M. D. Verweij, and K. W. van Dongen, “Modeling three-dimensional nonlinear acoustic wave fields in media with spatially varying coefficient of nonlinearity, attenuation and speed of sound,” in *2012 IEEE International Ultrasonics Symposium* (2012), pp. 519–522.

<sup>7</sup>A. Pulkkinen, B. Werner, E. Martin, and K. Hynynen, “Numerical simulations of clinical focused ultrasound functional neurosurgery,” *Phys. Med. Biol.* **59**(7), 1679–1700 (2014).

<sup>8</sup>P. B. Rosnitskiy, P. V. Yuldashev, O. A. Sapozhnikov, L. R. Gavrilo, and V. A. Khokhlova, “Simulation of nonlinear trans-skull focusing and formation of shocks in brain using a fully populated ultrasound array with aberration correction,” *J. Acoust. Soc. Am.* **146**(3), 1786–1798 (2019).

<sup>9</sup>C. Vanhille and C. Campos-Pozuelo, “Numerical and experimental analysis of strongly nonlinear standing acoustic waves in axisymmetric cavities,” *Ultrasonics* **43**(8), 652–660 (2005).

<sup>10</sup>E. Filonenko and V. Khokhlova, “Effect of acoustic nonlinearity on heating of biological tissue by high-intensity focused ultrasound,” *Acoust. Phys.* **47**(4), 468–475 (2001).

<sup>11</sup>I. M. Hallaj and R. O. Cleveland, “FDTD simulation of finite-amplitude pressure and temperature fields for biomedical ultrasound,” *J. Acoust. Soc. Am.* **105**(5), L7–L12 (1999).

<sup>12</sup>M. Solovchuk, T. W. Sheu, and M. Thiriet, “Simulation of nonlinear Westervelt equation for the investigation of acoustic streaming and nonlinear propagation effects,” *J. Acoust. Soc. Am.* **134**(5), 3931–3942 (2013).

<sup>13</sup>V. W. Sparrow and R. Raspet, “A numerical method for general finite amplitude wave propagation in two dimensions and its application to spark pulses,” *J. Acoust. Soc. Am.* **90**(5), 2683–2691 (1991).

<sup>14</sup>S. Ginter, M. Liebler, E. Steiger, T. Dreyer, and R. E. Riedlinger, “Full-wave modeling of therapeutic ultrasound: Nonlinear ultrasound propagation in ideal fluids,” *J. Acoust. Soc. Am.* **111**(5), 2049–2059 (2002).

<sup>15</sup>K. Fukuhara and N. Morita, “FDTD simulation of nonlinear ultrasonic pulse propagation in ESWL using equations including Lagrangian,” *Electr. Eng. Jpn.* **169**(4), 29–36 (2009).

<sup>16</sup>J. F. Kelly, S. Marras, X. Zhao, and R. J. McGough, “Linear and nonlinear ultrasound simulations using the discontinuous Galerkin method,” *J. Acoust. Soc. Am.* **143**(4), 2438–2448 (2018).

<sup>17</sup>B. E. Treeby and B. T. Cox, “ $k$ -Wave: MATLAB toolbox for the simulation and reconstruction of photoacoustic wave fields,” *J. Biomed. Opt.* **15**(2), 021314 (2010).

<sup>18</sup>Y. Jing, T. Wang, and G. T. Clement, “A  $k$ -space method for moderately nonlinear wave propagation,” *IEEE Trans. Ultrason. Ferroelectr.* **59**(8), 1664–1673 (2012).

<sup>19</sup>T. D. Mast, L. P. Souriau, D.-L. Liu, M. Tabei, A. I. Nachman, and R. C. Waag, “A  $k$ -space method for large-scale models of wave propagation in tissue,” *IEEE Trans. Ultrason. Ferroelectr.* **48**(2), 341–354 (2001).

<sup>20</sup>M. Hornikx, W. De Roeck, and W. Desmet, “Simplified exhaust pipe noise radiation modelling using the Fourier PSTD method,” *ISMA 2010*.

<sup>21</sup>Q. H. Liu and J. Q. He, “An efficient PSTD algorithm for cylindrical coordinates,” *IEEE Trans. Antennas Propag.* **49**(9), 1349–1351 (2001).

<sup>22</sup>S. Lin, “Modeling of borehole radar for well logging using pseudospectral time domain algorithm,” *J. Earth Sci.* **20**(6), 978–984 (2009).

<sup>23</sup>O. Bou Matar, V. Preobrazhensky, and P. Pernod, “Two-dimensional axisymmetric numerical simulation of supercritical phase conjugation of ultrasound in active solid media,” *J. Acoust. Soc. Am.* **118**(5), 2880–2890 (2005).

<sup>24</sup>C. Batifol, S. Callé, P. Maréchal, M. Lethiecq, and F. Levassort, “Pseudospectral time-domain method to calculate radiation pattern of lens-focused transducers,” in *IEEE Int. Ultra. Symp.* (2005), pp. 1660–1663.

<sup>25</sup>C. Bastard, J.-P. Remeniéras, S. Callé, and L. Sandrin, “Simulation of shear wave propagation in a soft medium using a pseudospectral time domain method,” *J. Acoust. Soc. Am.* **126**(4), 2108–2116 (2009).

<sup>26</sup>E. Filoux, S. Calle, R. Lou-Moeller, M. Lethiecq, and F. Levassort, “3-D numerical modeling for axisymmetrical piezoelectric structures: Application to high-frequency ultrasonic transducers,” *IEEE Trans. Ultrason. Ferroelectr.* **57**(5), 1188–1199 (2010).

<sup>27</sup>E. Wise, J. Jaros, B. T. Cox, and B. E. Treeby, “Pseudospectral time-domain (PSTD) methods for the wave equation: Realising boundary conditions with discrete sine and cosine transforms,” *arXiv:2005.00322* (2020).

<sup>28</sup>J. S. Mendousse, “Nonlinear dissipative distortion of progressive sound waves at moderate amplitudes,” *J. Acoust. Soc. Am.* **25**(1), 51–54 (1953).

<sup>29</sup>M. Tabei, T. D. Mast, and R. C. Waag, “A  $k$ -space method for coupled first-order acoustic propagation equations,” *J. Acoust. Soc. Am.* **111**(1), 53–63 (2002).

<sup>30</sup>R. E. Mickens, *Nonstandard Finite Difference Models of Differential Equations* (World Scientific, Singapore, 1994).

<sup>31</sup>B. T. Cox, S. Kara, S. R. Arridge, and P. C. Beard, “ $k$ -space propagation models for acoustically heterogeneous media: Application to biomedical photoacoustics,” *J. Acoust. Soc. Am.* **121**(6), 3453–3464 (2007).

<sup>32</sup>B. Treeby, E. Wise, and B. Cox, “Nonstandard Fourier pseudospectral time domain (PSTD) schemes for partial differential equations,” *Commun. Comput. Phys.* **24**(3), 623–634 (2018).

<sup>33</sup>J. Cheng, T. Alkhalifah, Z. Wu, P. Zou, and C. Wang, “Simulating propagation of decoupled elastic waves using low-rank approximate mixed-domain integral operators for anisotropic media,” *Geophysics* **81**(2), T63–T77 (2016).

- <sup>34</sup>B. Cox and B. Treeby, "Accurate time-varying sources in  $k$ -space pseudo-spectral time domain acoustic simulations," in *2018 IEEE International Ultrasonics Symposium (IUS)* (2018), pp. 1–4.
- <sup>35</sup>S. A. Martucci, "Symmetric convolution and the discrete sine and cosine transforms," *IEEE Trans. Signal Process.* **42**(5), 1038–1051 (1994).
- <sup>36</sup>M. Frigo and S. G. Johnson, *FFTW (User Manual)* (Massachusetts Institute of Technology, Cambridge, MA, 2018).
- <sup>37</sup>P. T. Christopher and K. J. Parker, "New approaches to the linear propagation of acoustic fields," *J. Acoust. Soc. Am.* **90**(1), 507–521 (1991).
- <sup>38</sup>J. L. Robertson, B. T. Cox, J. Jaros, and B. E. Treeby, "Accurate simulation of transcranial ultrasound propagation for ultrasonic neuromodulation and stimulation," *J. Acoust. Soc. Am.* **141**(3), 1726–1738 (2017).
- <sup>39</sup>B. E. Treeby and B. Cox, "A  $k$ -space Green's function solution for acoustic initial value problems in homogeneous media with power law absorption," *J. Acoust. Soc. Am.* **129**(6), 3652–3660 (2011).
- <sup>40</sup>E. S. Wise, B. Cox, J. Jaros, and B. E. Treeby, "Representing arbitrary acoustic source and sensor distributions in Fourier collocation methods," *J. Acoust. Soc. Am.* **146**(1), 278–288 (2019).
- <sup>41</sup>A. D. Pierce, *Acoustics: An Introduction to Its Physical Principles and Applications* (Acoustical Society of America, Melville, NY, 1990).
- <sup>42</sup>H. T. O'Neil, "Theory of focusing radiators," *J. Acoust. Soc. Am.* **21**(5), 516–526 (1949).
- <sup>43</sup>V. C. Anderson, "Sound scattering from a fluid sphere," *J. Acoust. Soc. Am.* **22**(4), 426–431 (1950).
- <sup>44</sup>R. A. Drainville, L. Curiel, and S. Pichardo, "Superposition method for modelling boundaries between media in viscoelastic finite difference time domain simulations," *J. Acoust. Soc. Am.* **146**(6), 4382–4401 (2019).
- <sup>45</sup>J. Gu and Y. Jing, "A modified mixed domain method for modeling acoustic wave propagation in strongly heterogeneous media," *J. Acoust. Soc. Am.* **147**(6), 4055–4068 (2020).
- <sup>46</sup>See <http://www.k-wave.org> (Last viewed 17 September 2020).
- <sup>47</sup>M. F. Hamilton and D. T. Blackstock, *Nonlinear Acoustics* (Acoustical Society of America, Melville, NY, 2008).